IN-47

NASA Contractor Report 191600

Science Support for the Earth Radiation Budget Experiment

James A. Coakley, Jr.
Oregon State University, College of Oceanic and Atmospheric Sciences, Corvallis, Oregon

FINAL REPORT

Science Support for the Earth Radiation Budget Experiment

NAS1-18992

James A. Coakley, Jr.

College of Oceanic and Atmospheric Sciences
Oregon State University
Corvallis, OR 97331-2209

A B S T R A C T

The work undertaken as part of the Earth Radiation Budget Experiment (ERBE) included the following major components: 1) The development and application of a new cloud retrieval scheme to assess errors in the radiative fluxes arrising from errors in the ERBE identification of cloud conditions. 2) The comparison of the anisotropy of reflected sunlight and emitted thermal radiation with the anisotropy predicted by the Angular Dependence Models (ADMs) used in to obtain the radiative fluxes. Additional studies included the comparison of calculated longwave cloud-free radiances with those observed by the ERBE scanner and the use of ERBE scanner data to track the calibration of the shortwave channels of the Advanced Very High Resolution Radiometer (AVHRR). Major findings included: 1) The misidentification of cloud conditions by the ERBE scene identification algorithm could cause 15% errors in the shortwave flux reflected by certain scene types. For regions containing mixtures of scene types, the errors were typically less than 5%. 2) The anisotropies of the shortwave and longwave radiances exhibited a spatial scale dependence which, because of the growth of the scanner field of view from nadir to limb, gave rise to a view zenith angle dependent bias in the radiative fluxes.

1. Introduction

Work undertaken as part of the ERBE project had four major thrusts: 1) the development and testing of new cloud retrieval schemes; 2) the use of the new retrieval schemes in validation studies of ERBE scene identification; 3) consistency checks between the observed anisotropy of the radiation fields and that derived from the ERBE Angular Dependence Models (ADMs) and 4) application of ERBE observations in radiation studies.

ERBE utilized scanner radiances to estimate the radiative energy budget of the earth-atmosphere system. Radiances observed by the scanner were converted to radiative fluxes through the application of anisotropic factors. Because the factors depended on the degree of cloudiness in the scene being viewed, a simple scheme was developed to determine the cloud conditions on the basis of the shortwave and longwave radiance pairs viewed by the scanner. The method became known as the ERBE Maximum Likelihood Estimation (MLE) scene identification method (Wielicki and Green, 1989). Errors in identification resulted, of course, in the application of inappropriate anisotropic factors which in turn led to erroneous estimates of reflected and emitted fluxes. The seriousness of these errors needed to be investigated.

When ERBE began, cloud retrieval algorithms were in their infancy. The procedures were rudimentary, arbitrary and physically unjustified. So, with the goal of assessing the errors that resulted from incorrect scene identification, new methods were sought for obtaining cloud cover from imagery data. The spatial coherence method (Coakley and Bretherton, 1982) grew out of this search. The method was used to assess errors in the ERBE MLE scene identification and resulting radiative fluxes. The spatial

1

coherence method is briefly described in Section 2 and the results of the scene identification validation studies are summarized in Section 3.

The ERBE V-5 data set of simultaneous ERBE, Advanced Very High Resolution Radiometer (AVHRR) and High Resolution Infrared Sounder (HIRS) observations was created to assess scene identification errors. The data set contained observations from ten minute orbital segments sampled every five days over twenty geographically distinct regions distributed around the globe. In addition to being used for scene identification validation, the V-5 observations have been used in several studies developing new retrieval methods, testing existing methods, characterizing the properties of particular cloud systems and calibrating the shortwave reflectivities obtained with the AVHRR. The calibration of AVHRR reflectivities is discussed in Section 8.

In addition to scene identification validation, the anisotropy of reflected and emitted radiances observed with the ERBE scanner on the ERBS satellite were compared with that derived from the anisotropic factors used by ERBE to obtain the radiative fluxes from the observed radiances. The comparisons were undertaken in order to estimate errors incurred through the use of inaccurate ADMs. As discussed in Section 4 the observed anisotropy was found to be a function of the spatial scale of the observations (Baldwin and Coakley, 1991). Because of the spatial-scale dependence, the anisotropic factors applied to fields of view at nadir were inconsistent with those applied for fields of view near the limb. Errors in scene identification coupled with the nonuniform spatial distribution of cloud systems and the growth of the field of view size from nadir to limb produced a bias in the ERBE radiative fluxes that depended on satellite zenith angle. The bias led to estimates of the global average albedo that depended on satellite zenith angle (R. Davies, Minutes ERBE Scince Team Meeting 22, ERBE Document 3-3-9-22-88; Suttles et al. 1992). As discussed in Section 5, the bias was discovered by using the

2

ERBS scanner observations to construct observations that held the area viewed constant for all viewing angles (Ye, 1993).

ERBE scanner observations were used to compare calculated and observed longwave radiances for clear land and ocean scenes (Stone, 1990; Stone and Coakley, 1990). The purpose of the study was to assess the feasibility of using conventional analyses of temperature and humidity profiles in radiative transfer models, like those used in general circulation climate models, to estimate the longwave fluxes. The results of the study are described in Section 7.

2.   Development of Cloud Retrieval Algorithms

In ERBE, radiances observed by the scanner were converted into radiative fluxes through the application of anisotropic factors (Suttles et. al., 1988). The angular dependence of reflected and emitted radiances depends on scene type. Radiances from overcast scenes are more isotropic than radiances from clear scenes. ERBE used the shortwave and longwave radiance pairs in a maximum likelihood estimation (MLE) scheme to determine the degree of cloud cover for the scene (Wielicki and Green, 1989). The accuracy of the retrieved fluxes depended on the reliability of the scene identification and on the accuracy with which the anisotropic factors allowed for the angular dependence of the reflected and emitted radiances associated with the scene. The only means of verifying the selection of scene type and associated anisotropy was to identify the scene through independent means using observations that were expected to be better than those obtained with the ERBE scene identification method. The obvious candidates for verifying scene types were retrievals obtained with the AVHRR and HIRS data that were collected with the ERBE scanner observations for the NOAA-9 and NOAA-10

satellites. The ERBE V-5 data product, as was mentioned above, was constructed to facilitate ERBE-AVHRR and HIRS comparisons.

When ERBE began, however, rudimentary threshold (Koffler et al., 1973) and visible-infrared bispectral methods (Reynolds and Vonder Haar, 1977) were the only means for obtaining cloud properties from satellite imagery data. The threshold routines were suspected of being flawed as they assumed that the clouds filled the field of view of the instrument, an unlikely occurrence for the AVHRR 4-km field of view (Shenk and Salomonson, 1972). The bispectral methods required *a priori* knowledge of the cloud radiative properties, which vary widely and are often unpredictable. The retrieval scheme used for the HIRS sounder observations, which has become known as the CO_2 slicing method, seemed to work for upper-level clouds but was clearly inadequate for low-level cloud systems--the systems which dominate ocean scenes (Wielicki and Coakley, 1981). So, new methods were sought for obtaining cloud properties from the available satellite observations.

The spatial coherence method for obtaining cloud properties from satellite imagery data (Coakley and Bretherton, 1982) grew out of a study which was originally designed to explore the limitations of threshold methods. The method distinguishes itself from threshold methods in that it avoids the assumption that clouds must fill the field of view of the sensor. Like the bispectral methods, the spatial coherence method relies on an assumption concerning cloud optical properties. The assumption is that pixels exhibiting uniform thermal emission are overcast by opaque layered clouds. This assumption appears to be valid (Wielicki and Parker, 1992). The assumption, in any case, is much less stringent than assumptions used in bispectral methods concerning the reflectivities of particular cloud systems. Cloud reflectivities are highly variable and seemingly unpredictable (Coakley and Bretherton, 1982).

The spatial coherence method relies on clouds forming in well-defined layers that extend over hundreds of kilometers. It identifies these layers on the basis of the local spatial structure of emitted radiances at 11-μm. Imager pixels that are overcast by clouds from distinct layers or pixels that are cloud-free exhibit a high degree of spatial uniformity. Figure 1 illustrates a spatial coherence analysis. The figure shows 11-μm radiances obtained for a 250 km region over the Pacific Ocean for the NOAA-9 overpass on 27 April 1985. The observations are from the ERBE V-5 data product. Pixels in the feet of the arch (open circles) with radiances near 102 mWm^{-2}sr^{-1}cm are associated with the cloud-free background. Those with radiances near 25 mWm^{-2}sr^{-1}cm are associated with an upper-level, layered cloud system. Points in the body of the arch represent radiances from pixels in which the clouds are evidently broken on the 4-km scale of the observations. Figure 2 shows 0.63-μm reflectivities and 11-μm radiances for the same system. The results indicate that the pixels found to be overcast by the spatial coherence method have high reflectivities, as would be expected for clouds that are opaque at 11 μm. Pixels which are found to be cloud-free have low reflectivities.

For single-layered systems, like that shown in Fig. 1, the cloud cover is obtained by assuming that all of the clouds are opaque at 11 μm. For a single layer of opaque clouds the radiances observed at 11-μm are given by

$$I = (1 - A_c)I_s + A_c I_c \tag{1}$$

where I_s is the radiance associated with the cloud-free portion of the scene, i.e., 102 mWm^{-2}sr^{-1}cm in the case of the observations shown in Fig. 1, I_c is the radiance associated with the overcast portion of the scene, i.e. 25 mWm^{-2}sr^{-1}cm in Fig. 1, and A_c is the fractional cloud cover. Cloud cover for any pixel is obtained by inverting (1) using
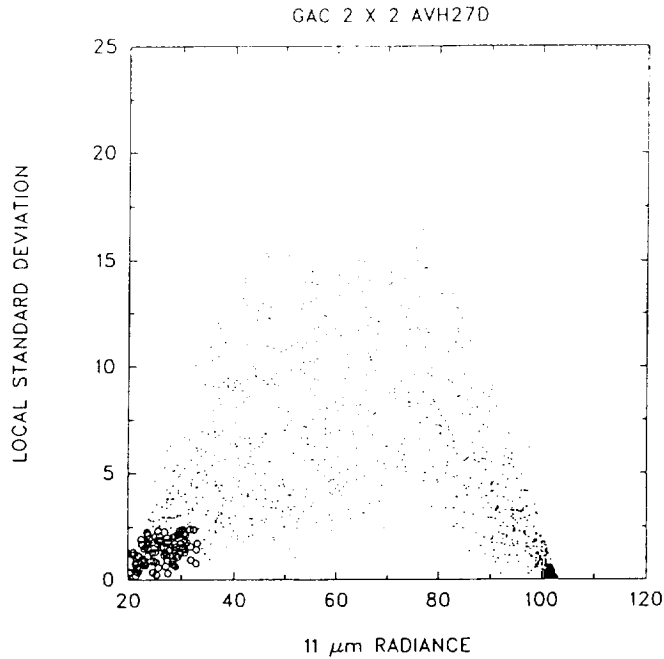
5

GAC 2 X 2 AVH27D

Figure 1. Spatial coherence analysis of 250 km region from the central Pacific V-5 region 1197 for the NOAA-9 pass on the afternoon of April 27, 1985. Each point in the figure indicates the mean and standard deviation of the 11-μm radiances (mWm^{-2}sr^{-1}cm) for 2 $\times$ 2 scan line $\times$ scan spot arrays of the 4-km GAC pixels. The pixels found to be cloud-free and overcast by the spatial coherence method are indicated by open circles.
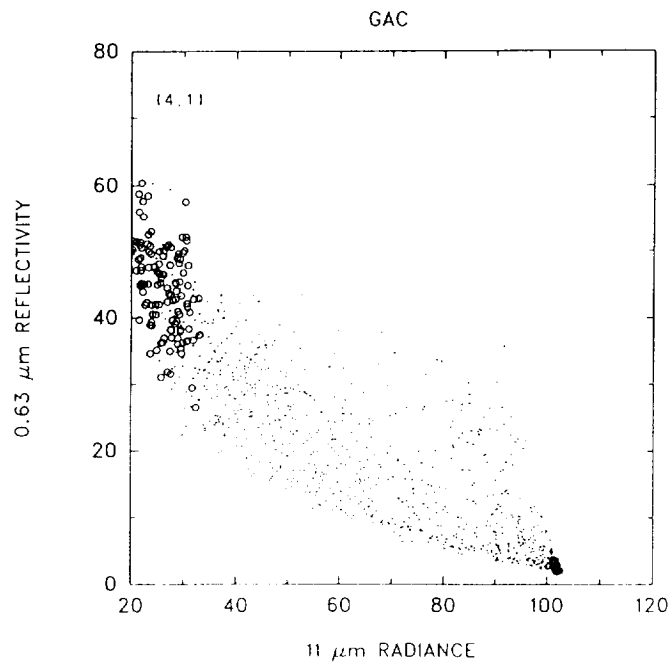
GAC

Figure 2. 0.63-μm reflectivities and 11-μm radiances for same region as that shown in Fig. 1.

I, the radiance observed for the pixel along with I_s and I_c obtained through spatial coherence analysis. For multi-leveled systems, the cloud cover is bracketed by assuming all clouds are either in the upper or lower layer determined through spatial coherence analysis or indicated by the extremes of the 11-μm radiance distribution (Coakley and Baldwin, 1984). As discussed in the next section, the spatial coherence method was used to examine the cloud scene types obtained with the ERBE MLE method.

In addition to providing data with which to verify the ERBE scene identification method, the ERBE V-5 data product has been used as a test bed for the development of cloud retrieval algorithms. Chang and Coakley (1993) used it to illustrate potential biases in cloud amount obtained with threshold methods and to develop simple procedures for estimating these biases. Among the results presented were distributions of cloud cover for 60 km and 250 km regions containing single-layered cloud systems over oceans. The populations of clear and overcast scenes at the 60 km (~20%) and 250 km (<5%) scales were not unlike those obtained with the ERBE MLE scene identification method (Baldwin and Coakley, 1991).

Lin and Coakley (1993) used V-5 observations to develop a multispectral infrared retrieval scheme for obtaining the cloud properties associated with single-layered systems in which some of the clouds were semitransparent at infrared wavelengths. The scheme avoids the opaque cloud approximation used in the spatial coherence method. Luo et al. (1994) applied the retrieval to marine stratocumulus found in V-5 region 1566 off the west coast of South America. The results indicated that a substantial fraction of the area covered by marine stratocumulus were semitransparent and thus the spatial coherence estimate of cloud cover, as given by inverting (1), underestimates the actual cover by 0.1 – 0.2. The results agreed with the study by Wielicki and Parker (1992) who, through the

analysis of ~120 m resolution Landsat imagery data, found that the spatial coherence method underestimated the fractional cloud cover by 0.18.

3.   Scene Identification Validation

The spatial coherence method was applied to the AVHRR observations in the ERBE V-5 data that were set aside for the validation of the ERBE MLE scene identification. For each ERBE scanner field of view, the AVHRR observations within the field of view were analyzed and the results convolved with the scanner point spread function. The scanner point spread function was obtained from R. Arduini (private communication). It was approximated by

$$f(\vartheta,\varphi) = N\exp\left(-\left[\left(\frac{\vartheta}{A}\right)^2 + \left(\frac{\varphi}{B}\right)^2\right]\right)$$
(2)

where ϑ is the along-track angular distance measured from the center of the scanner axis, φ is the across-track angular distance, N is a normalization factor, $A = 1.9°$ and $B = 2.3°$. The satellite zenith angle recorded in the S8 data stream was used to indicate the pointing position of the scanner.

The quality of the model for the point spread function and the mapping of the AVHRR pixels into the ERBE pixels was assessed through correlations between the ERBE shortwave and longwave radiances with the AVHRR narrow band counterparts and through the comparison of images made from the ERBE shortwave and longwave radiances with those simulated by convolving the AVHRR radiances with the scanner point spread function. Figure 3 shows typical correlations for the shortwave and
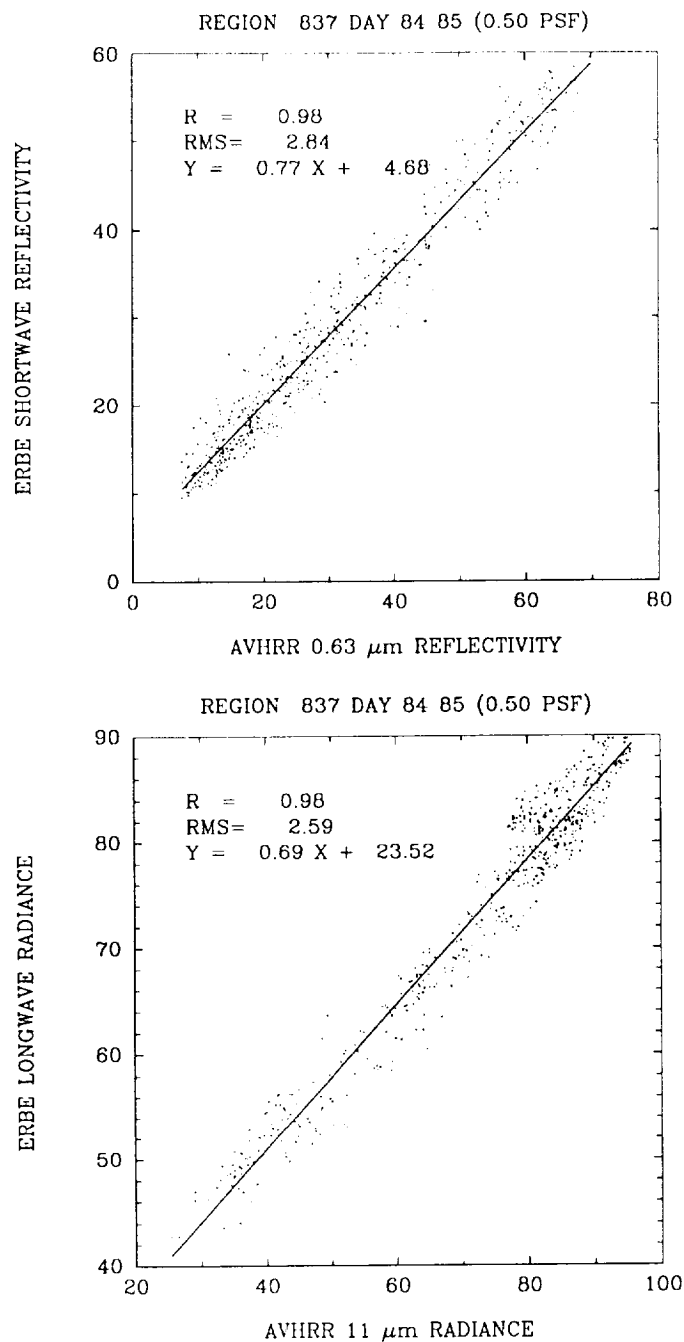
8

Figure 3. Correlation of AVHRR narrow-band reflectivities and radiances to ERBE shortwave and longwave reflectivities and radiances. Observations are for ERBE V-5 region 837 in the northeastern Pacific on 25 March 1985. Each point in the figure represents the values for a single ERBE scanner field of view. Only fields of view identified as partly cloudy, mostly cloudy and overcast are shown.

longwave radiances for partly cloudy, mostly cloudy and overcast scenes taken from the V-5 region 1197 in the central Pacific. The high degree of correlation indicates that the model used for the point spread function was an adequate representation.

The spatial coherence analysis of the AVHRR observations within each of the ERBE scanner fields of view provided the cloud cover for each of the scanner fields of view. The cloud cover was used to determine the cloud scene type using the range of cloud cover said to be associated with each of the ERBE scene types. For the majority of scenes, the identification obtained from the spatial coherence analysis of the imagery pixels agreed with that obtained by the ERBE MLE scene identification. Table 1 shows the percent occurrence of scene types identified by the spatial coherence method and the ERBE MLE method for all ocean scenes for the month of April 1985. The table also shows the mean of the reflected fluxes for each scene type obtained by applying the appropriate anisotropic factor to each ERBE scanner field of view. The spatial coherence method found more clear scenes than did the ERBE MLE method, but it also found fewer overcast scenes. The major difference between the two methods was that the ERBE MLE often identified upper-level clouds as being overcast or mostly cloudy when the spatial coherence method identified these systems as being only mostly or partly cloudy. Consequently, the average reflected fluxes for mostly cloudy and overcast scenes were higher for the scenes identified by the spatial coherence method. To some extent these tendencies were compensated through the allowance of more cloud contamination in the clear scenes by the spatial coherence method. The average of the reflected flux for the clear scenes was higher for the scenes identified by the spatial coherence method. There was also some compensation due to the underestimate of cloud cover for low-level systems by the ERBE MLE (Coakley, 1990). While large differences in the reflected fluxes occurred for some of the scene types, the average reflected flux for all scene types was within 5% for the two scene identification schemes.

Table 1. Spatial Coherence and ERBE MLE scene identification for ocean scenes in April 1985.

Scene Type	Spatial Coherence		ERBE MLE	
	Percent Occurrence	Average Reflected Flux (Wm^{-2})	Percent Occurrence	Average Reflected Flux (Wm^{-2})
Clear	22	99	17	92
Partly-cloudy	42	189	33	162
Mostly-cloudy	27	365	32	289
Overcast	9	525	18	441
All Scenes	100	247	100	239

As was noted above, the scene type obtained for the spatial coherence method was based on the assignment of the retrieved fractional cloud cover to ERBE scene type according to the conventional definitions of the ERBE scene types. This assignment was, of course, arbitrary and the scene types identified by the spatial coherence method may well be inconsistent with those obtained by the ERBE MLE. The scene types associated with the ERBE MLE were obtained from NIMBUS-7 Earth Radiation Budget (ERB) observations in which the scene types were determined on the basis of multiple thresholds applied to the Temperature Humidity Infrared Radiometer (THIR) imagery data (Taylor and Stowe, 1984; Suttles et al., 1988). Efforts were begun to assess the effect of selecting different scene types on the anisotropy of the reflected and emitted radiances. Figure 4 shows reflected and emitted radiances for scenes identified separately by the
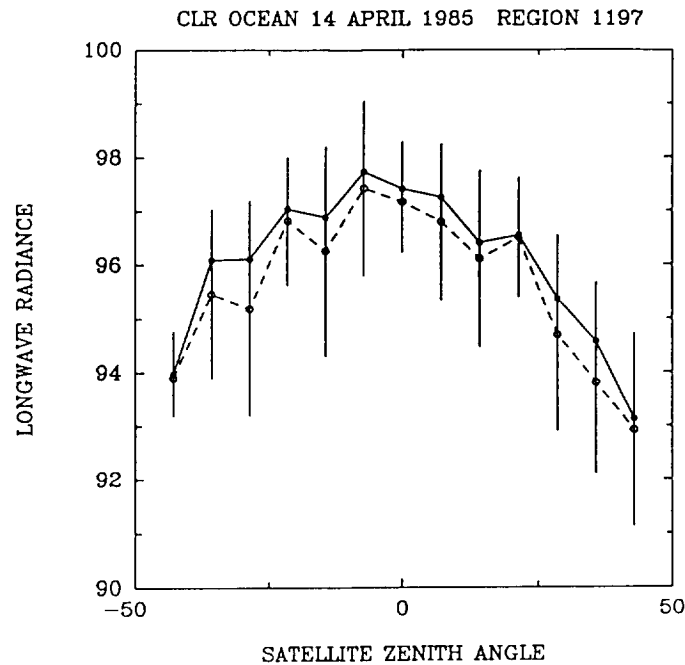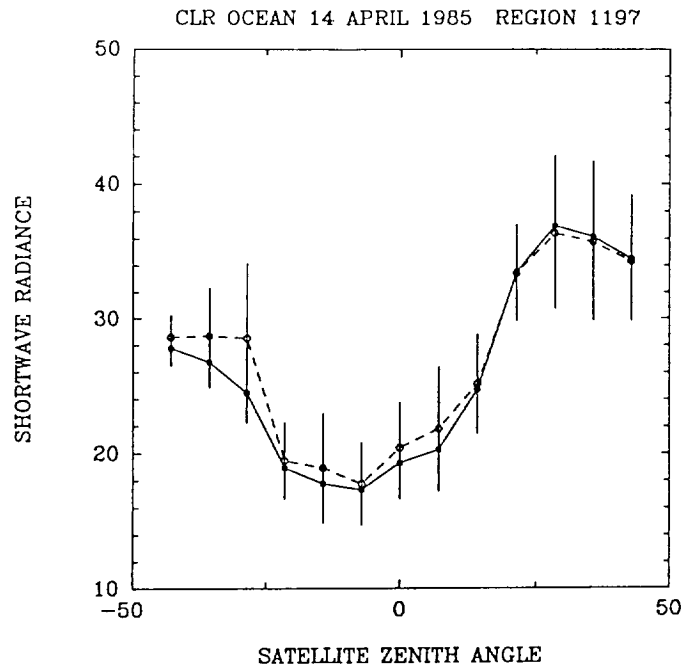
Figure 4. Shortwave and longwave radiances (Wm⁻²sr⁻¹) for clear scenes identified by the ERBE MLE (solid line, dots) and by the spatial coherence method applied to collocated AVHRR observations (open circles, dashed lines). The points represent the means of the radiances; the error bars represent the standard deviations. The results illustrate the good agreement in the anisotropy observed for clear scenes. They also suggest that the spatial coherence method tolerates slightly more cloud contamination than does the ERBE MLE. The observations are for the afternoon pass of NOAA-9 over ERBE V-5 region 1197 in the central Pacific.

ERBE MLE method and the spatial coherence method as being clear ocean scenes. The figure shows that for clear scenes the observed radiances are in good agreement. Differences in the observed anisotropy appear to be within the variability of the radiances observed for such scenes. The higher reflectivities and lower emitted radiances obtained with the spatial coherence scene identification illustrate the effect of the less stringent clear sky conditions of the spatial coherence method.

4.   Consistency of Observed Anisotropy and ERBE Angular Dependence Models.

Baldwin and Coakley (1991) used ERBS scanner observations to determine whether the anisotropy of reflected sunlight for the various scene types was consistent with that derived from the ERBE Angular Dependence Models (ADMs) used to derive radiative fluxes from the observed radiances. Differences were anticipated because in ERBE, scene types were identified on the basis of the longwave-shortwave radiance pair for the field of view in question. Since longwave and shortwave radiances appeared to be nonlinearly related, the relationship between the radiance pairs changed depending on the size of the region being observed. In other words, the relationship was a function of field of view size. The radiance pairs used in the ERBE MLE scene identification and in the ADMs were derived from radiances obtained with the NIMBUS-7 scanner which had a nadir field of view size of ~ 90 km. The ERBE scanner had a field of view that was approximately half the NIMBUS-7 field of view size at nadir. The difference in field of view size alone should have given rise to differences. Other factors that could have contributed were the differences in the radiometric calibration between the NIMBUS-7 and ERBE radiometers and differences in the scene identification methods used to extract the ADMs from the NIMBUS-7 observations and to apply them in ERBE.

Baldwin and Coakley (1991) found systematic differences between the anisotropy observed with the ERBE scanner and that derived using the ERBE ADMs. Figure 5 shows percent differences in the pseudo-anisotropic factors found for April 1985 based on observations from the ERBS scanner. The pseudo-anisotropic factor is given by

$$\rho_{ijkl} = \frac{\langle I_{ijkl} \rangle}{\sum_{jk} \mu_j \langle I_{ijkl} \rangle \Delta\mu_j \Delta\varphi_k} \tag{3}$$

where i indicates the scene type, j indicates the satellite zenith angle bin, k indicates the relative azimuth angle bin, l indicates the solar zenith angle bin and $\langle I_{ijkl} \rangle$ represents the mean radiance for the associated model type and angular bins. The summation in the denominator of (3) includes only those angular bins for which a sizable number of observations were obtained (~ 40). Were it to include all bins, the denominator would become the reflected flux for the particular scene type and solar zenith angle. Because of restrictions in viewing geometries imposed by the ERBS orbit, some bins had few or no observations. The pseudo-anisotropic factor was employed as a means of allowing for bins with insufficient observations. The pseudo-anisotropic factors were also derived from the ERBE ADMs using the same ensemble of scene types and viewing geometries.

The percent differences in the pseudo-anisotropic factors derived from the scanner observations and from the ERBE ADMs were typically 5-10%. Figure 5 shows results for the ocean scenes for the solar zenith angle bins that exhibited the largest angular domain of significant differences. The shaded areas in the figures represent the domain for which the differences in the pseudo-anisotropic factor were statistically significant at the ~ 90% confidence level. The significance was determined by taking the mean radiances in each
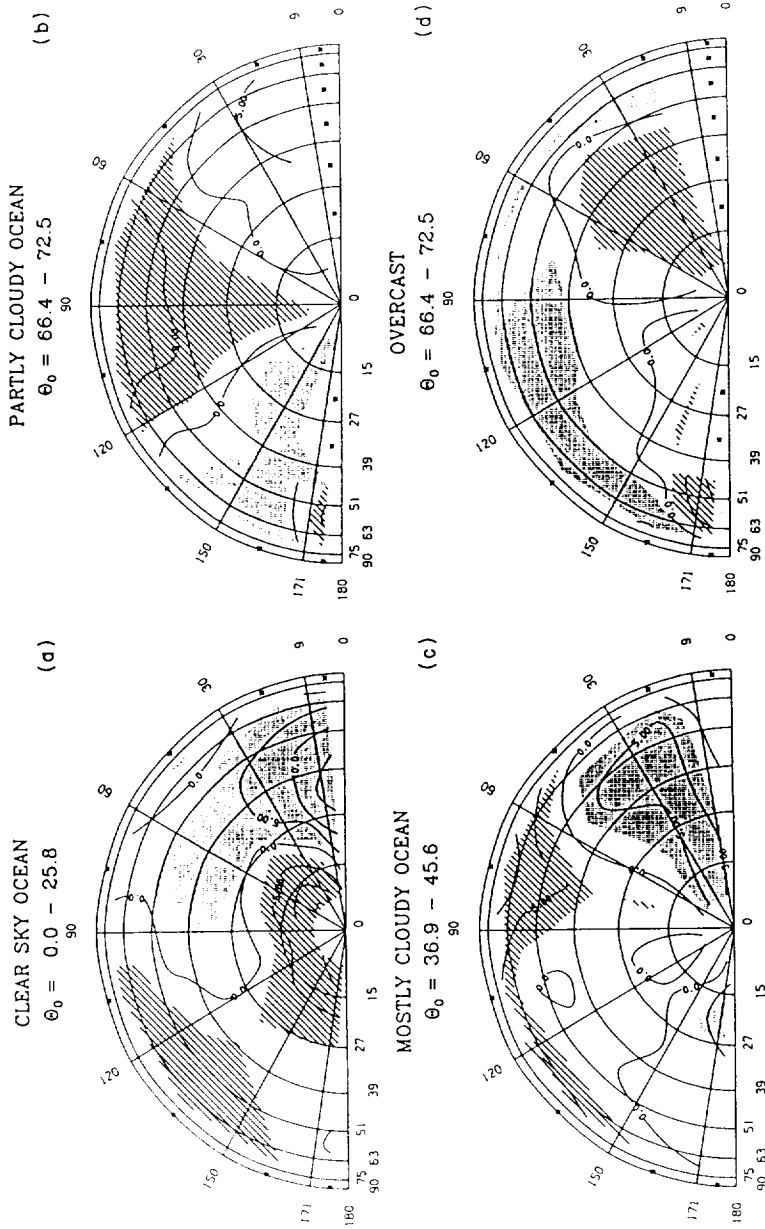
Figure 5 Percent differences in psuedo-anisotropic factors, $100 \times \left(\text{ERBE ADM} - \text{Observed} \right) / \text{ERBE ADM}$, derived from ERBS scanner observations for April 1985. The contour intervals are 5%. The shaded regions indicate differences that are statistically significant at the 90% confidence level.

15

model-angular bin for sets of 40 consecutive ERBS scan lines as being independent estimates of the mean within the particular bin. The area covered by 40 ERBS scan lines is ~ 2000 km. The size of the region was chosen so that the ratio of the differences in the anisotropic factors to the standard deviations of the factors were relatively insensitive to the number of scan lines for which the averages were constructed.

Baldwin and Coakley (1991) used the discrepancies between the observed anisotropy and that derived from the ERBE ADMs to estimate errors in the monthly mean $2.5° \times 2.5°$ latitude $\times$ longitude average fluxes. They found that were the ERBE ADMs to be consistent with the observed anisotropy, the rms errors in the fluxes would be ~ 4 % which compares favorably with ~ 15 % obtained by ignoring the anisotropy of the radiation field and assuming that the reflected sunlight is isotropic. The bias errors would be almost negligible when using ADMs that are consistent with the observed anisotropy as opposed to ±4% assuming isotropy.

5.   Spatial-scale Dependence of Observed Anisotropy

Ye (1993) extended the work of Baldwin and Coakley (1991) by exploring the spatial scale dependence of the observed anisotropy. Radiances were averaged for ERBE scanner fields of view near nadir in order to construct observations which maintained a relatively constant spatial scale as the satellite nadir view angle swept from nadir to limb. The radiances from these constant size field of view observations were compared with those at full resolution to detect differences in the anisotropy of reflected and emitted radiances with differences in spatial scale. Scene identification for the constant size field of view observations was obtained by averaging the MLE cloud fraction for the scanner fields of view contributing to the particular constant size field of view and then assigning the scene type associated with the particular average cloud fraction. Only constant size

field of view observations having a homogeneous geographic scene type (e.g. land or ocean) were analyzed. Pseudo-anisotropic factors were obtained for both the constant size field of view observations and the full resolution scanner data. Ye (1993) found significant systematic differences not unlike those shown in Fig. 5 in the anisotropic factors thereby demonstrating that the observed anisotropy was a function of spatial scale.

This spatial scale dependence was anticipated. First, the MLE scene identification is subject to errors. Clear scenes have, to varying degrees, some cloud contamination. Likewise, overcast scenes have, to varying degrees, some clear contamination. Second, cloud systems are not uniformly distributed in space. Instead, they cluster so that clear regions ~ 40 km in scale, i.e. the size of a full resolution scanner field of view at nadir, are often found in the midst of extensive, broken cloud systems. Such regions, when viewed by the ERBE scanner and identified as being clear have a relatively high probability of being cloud contaminated. Clear regions that are ~ 100 km scale, i.e. the size of an ERBE scanner field of view near the limb, are typically found in large-scale regions that are extremely clear. Fields of view identified as clear for such regions have a low probability of being cloud contaminated. The converse follows for the contamination of overcast scenes with clear areas. Consequently, because of errors in the MLE scene identification, the growth of the scanner field of view size from nadir to limb and the clustering of clouds within certain spatial scales, ERBE fluxes are subject to a satellite zenith angle dependent bias.

Because ~ 100 km scale clear regions tend to be very clear (and similarly ~ 100 km scale overcast regions tend to be completely overcast) and because radiances reflected from clear scenes tend to be more anisotropic than those reflected by overcast scenes, the pseudo anisotropic factors constructed for clear scenes from the constant size field of view observations were expected to exhibit stronger anisotropy than those constructed from the

17

full resolution scanner observations. Conversely, the pseudo anisotropic factors for the overcast scenes were expected to exhibit less anisotropy. Figure 6 shows the pseudo anisotropic factors averaged over azimuth and solar zenith angles for the constant size fields of view and the full resolution ERBE scanner observations. The radiances reflected from the clear regions for the constant size fields of view were indeed slightly more anisotropic than those for the full resolution observations as expected. Those for the overcast scenes, however, were also more anisotropic countering expectations. The failure of the overcast scenes to behave as expected led Ye to search for evidence of gross errors in the ERBE MLE scene identification.

Ye obtained the frequency of occurrence of scene types for the constant size field of view observations for the months of September, October and November, 1985. Because the area covered by the constant size field of view observations is relatively independent of satellite zenith angle, the frequencies of occurrence for the various scene types, sampled over the globe and for a sufficiently long period of time, should be independent of satellite zenith angle. Figure 7 shows the frequencies of occurrence for the constant size field of view observations. Only the clear scenes exhibit the required constant frequency. The frequency of overcast scenes increases with satellite zenith angle indicating gross errors in the MLE identification.

Ye developed a simple threshold scene identification scheme to rectify the errors in the ERBE MLE identification method. The MLE scene identification was assumed to provide accurate scene identification at nadir. Thresholds for shortwave and longwave radiances were adjusted so that for the constant size field of view observations the frequency of scene types remained reasonably constant with satellite zenith angle. These thresholds were applied to both full resolution ERBS scanner observations and the constant size field of view observations. Differences in the anisotropy of the reflected

SZA 0.0 - 90.
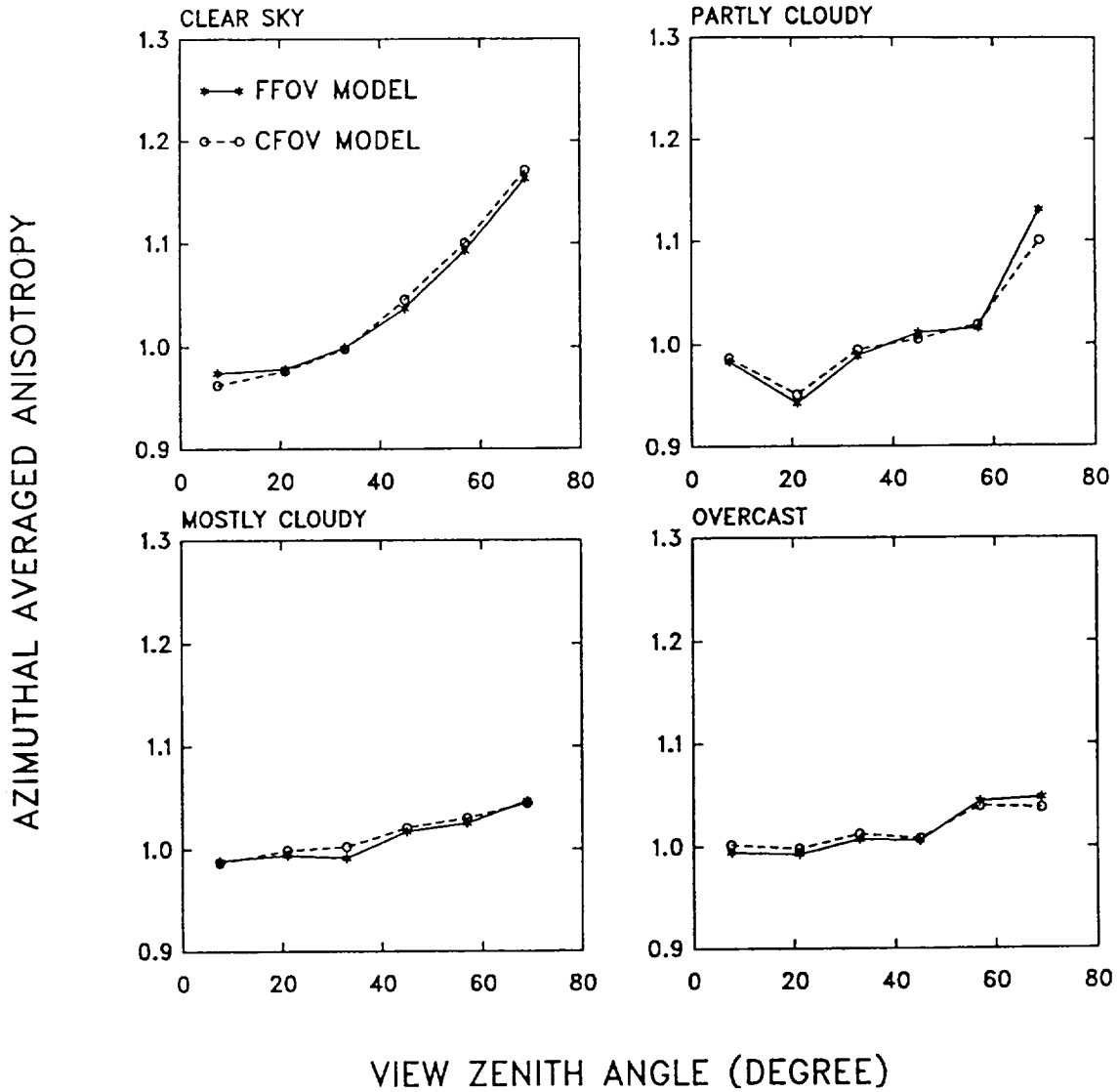
Figure 6. Psuedo anisotropic factors averaged over azimuth and solar zenith angles for full resolution ERBE scanner observations (FFOV) and constant size field of view observations (CFOV). The observations were derived from the ERBS scanner data for September, October and November 1986.
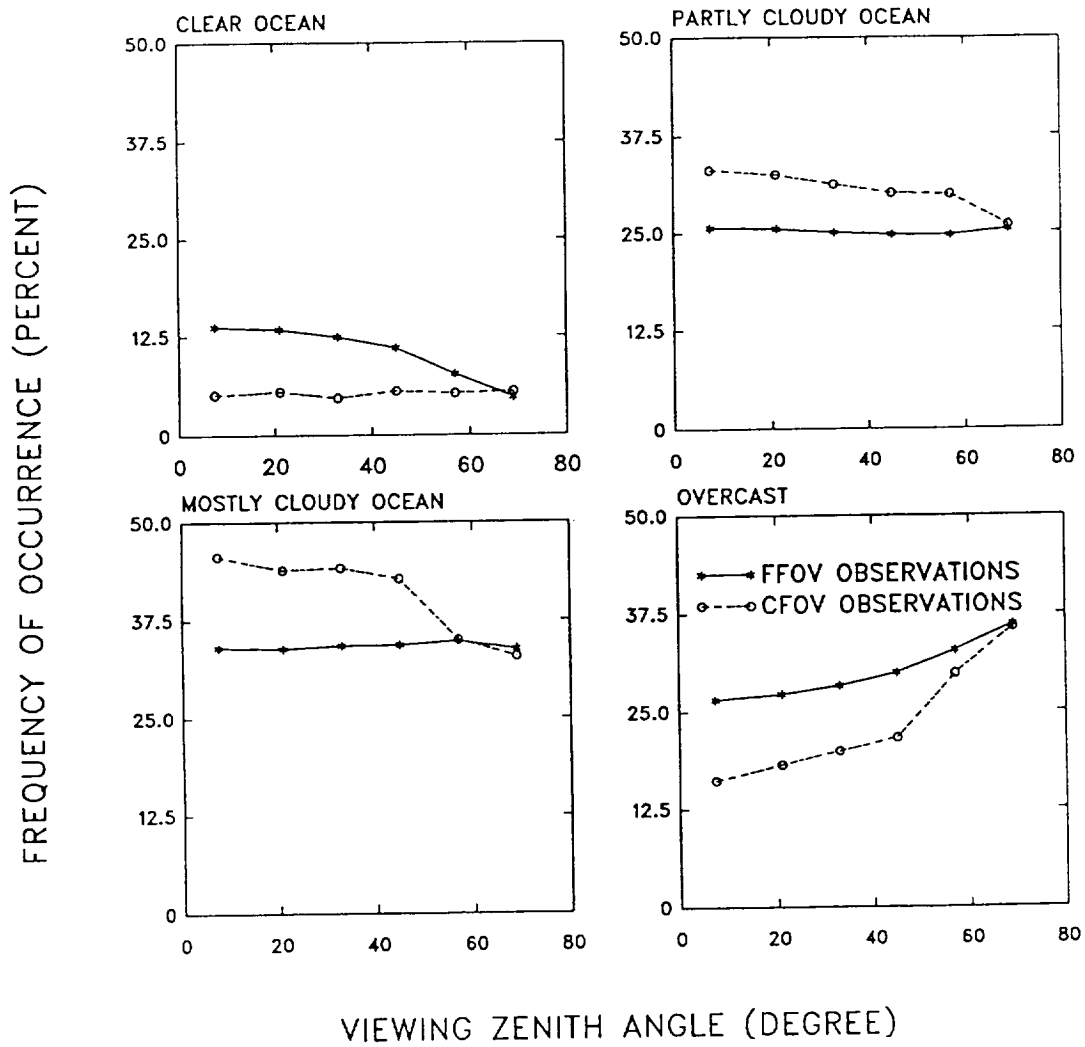
Figure 7. Frequencies of occurrence for the constant size field of view (CFOV) and full resolution (FFOV) ERBE scanner observations. The observations are from the ERBS scanner data for September, October and November 1986.

radiation for the various scene types for the full resolution and constant size field of view observations were found to be insignificant thereby demonstrating that a procedure could be developed for obtaining anisotropic factors from radiances observed with scanning radiometers once allowance was made for the apparent spatial scale dependence of the anisotropy and the growth of the field of view size from nadir to limb.

Ye used the constant size field of view observations to evaluate new ADMs and used the ADMs to re-evaluate the reflected and emitted fluxes obtained with the ERBS satellite. In addition, he developed a second threshold scene identification scheme in which full resolution ERBE scanner fields of view were subjected to thresholds which gave the proper population of scene types for the areas associated with the full resolution scanner field of view at the various satellite viewing angles. These observations were referred to as the full resolution (FFOV) threshold observations. A long-standing problem (R. Davies, Minutes ERBE Scince Team Meeting 22, ERBE Document 3-3-9-22-88; Suttles et al. 1992) was that the global average albedo obtained by averaging observations at a fixed satellite zenith angle depended on the zenith angle. Ye found that with the new constant size field of view ADMs and threshold scene identification, the satellite zenith angle dependence of the global average albedo was statistically insignificant. Figure 8 shows the global average albedo obtained using the ERBE MLE, the constant size field of view (CFOV) and the modified full resolution threshold observations (FFOV) as a function of satellite zenith angle.

ERBE estimates of the global energy budget indicated that the earth absorbed about 5 Wm^{-2} than it emitted (Harrison et al. 1990). Based on the relative magnitudes of the CFOV and ERBE MLE estimates of the global average albedo for September, October and November, 1986, Ye estimated that the albedo for the CFOV observations was 3% higher than that obtained with the ERBE MLE. The higher albedo would bring the earth closer to radiative equilibrium. For the ERBS observations, the earth absorbs

ESTIMATED SPHERICAL ALBEDO

Figure 8. Global average albedo obtained using the ERBE MLE and ADMs, the threshold scene identification and associated ADMs for the full resolution scanner observations (FFOV) and for the constant size field of view (CFOV) observations. The results are based on ERBS scanner observations for September 1986.
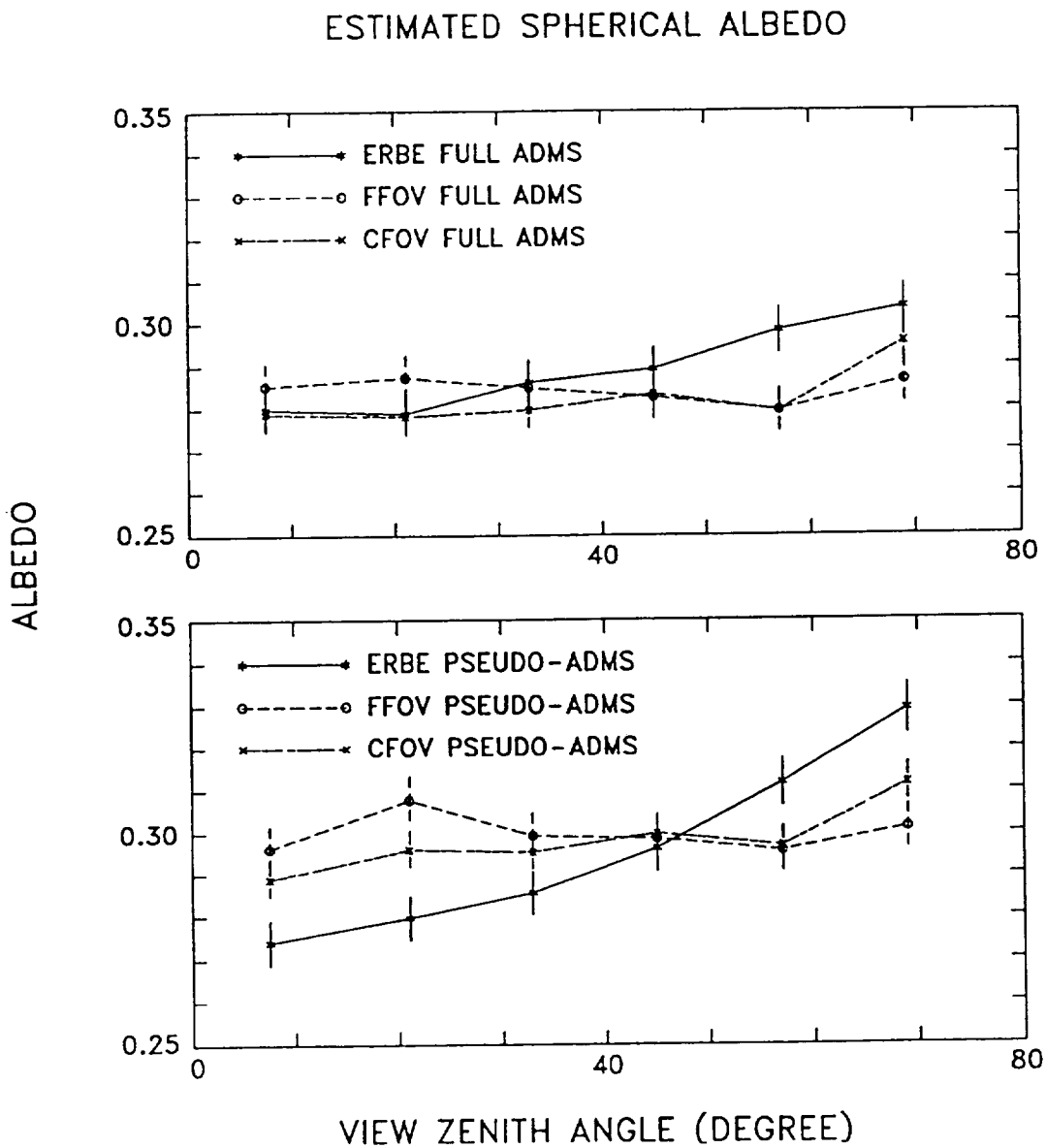
about 3.3 Wm^{-2} more sunlight than it emits to space when the ERBE MLE identification and ADMs are used; it emits about 0.9 Wm^{-2} more than it absorbs when the CFOV threshold identification and ADMs are used.

6.   Calculated and Observed Cloud-Free Longwave Radiances

Stone (1990) and Stone and Coakley (1990) compared observed broadband longwave radiances obtained with the ERBS scanner for clear scenes and those calculated using NMC analyses of temperature and humidity profiles in a radiative transfer model. The purpose of the study was to explore the feasibility of using analyzed meteorological fields to compute radiances using a radiative transfer scheme not unlike those in many general circulation climate models.

The radiative transfer model was a modified version of the Rogers and Walshaw (1966) band model scheme (Stone, 1990). The model included absorption by water vapor, ozone and carbon dioxide. It did not allow for absorption by the minor trace species such as the CFCs, methane and nitrous oxide. Longwave fluxes obtained with the model were found to be higher by about 3% than those obtained with a line-by-line radiative transfer code in which the effects of only water vapor, ozone and carbon dioxide were included (Luther et al., 1988).

ERBS scanner observations within ±30 minutes of 0Z and 12Z for July 1985 and January 1986 were analyzed for 3 × 3 scan line × scan spot arrays of scanner fields of view in which all of the fields of view were identified as being clear. Temperature and humidity profiles from the 0Z and 12Z NMC analyses were spatially interpolated to the location of the ERBS scanner observation. The radiance associated with the center of the 3 × 3 field of view array was calculated using the analyzed fields. In the calculations, ozone mixing

23

ratios were taken from Krueger and Minzner (1976). Climatological values for temperature were used for layers above 50 mb and for water vapor above 300 mb.

Results of the comparisons are given in Table 2. The calculated radiances underestimate the observed radiances by 2 – 4 % for most of the globe. Over land and deserts, however, the underestimate can reach 10%. The discrepancies over land appear to be linked to the diurnal cycle of the surface temperature which is not allowed for in the NMC analyses. Figure 9 shows the unfiltered longwave radiances observed by the ERBS scanner, percent differences between observed and calculated radiances and the surface air temperatures from the NMC analyses. The observations are for clear scenes in July 1985 for all land areas in the latitude range 30°N – 60°N. The peak in the differences between observed and calculated longwave radiances coincides with the peak surface air temperature. The surface skin temperature at the peak is probably even higher than the surface air temperature. Allowance for the skin temperature would probably reduce the differences between the observed and calculated longwave radiances.

7.   Calibration of AVHRR Shortwave Radiances

During the FIRE Marine Stratocumulus Intensive Field Observations (IFO) in July 1987, observations of cloud liquid water based on microwave radiances obtained with a surface-based radiometer were compared with reflectivities of extensive overcast layered clouds obtained from the NOAA-9 and NOAA-10 AVHRRs in order to test parameterizations for cloud reflectivity often used in general circulation climate models. In this case, the Stephens (1978) parameterization was tested. Figure 10 shows the observed and expected reflectivities as a function of liquid water path (Coakley and Snider, 1989). The disagreement was spectacular. Attempts to explain the disagreement through allowing for the absorption of ozone in the bandpass of the AVHRR, nonzero
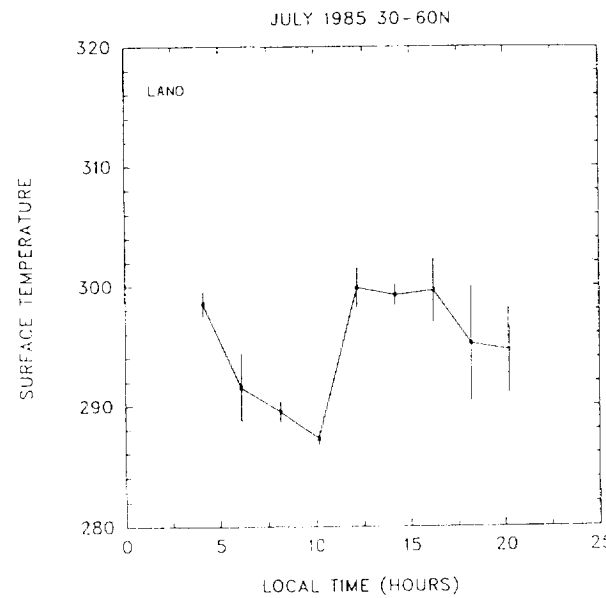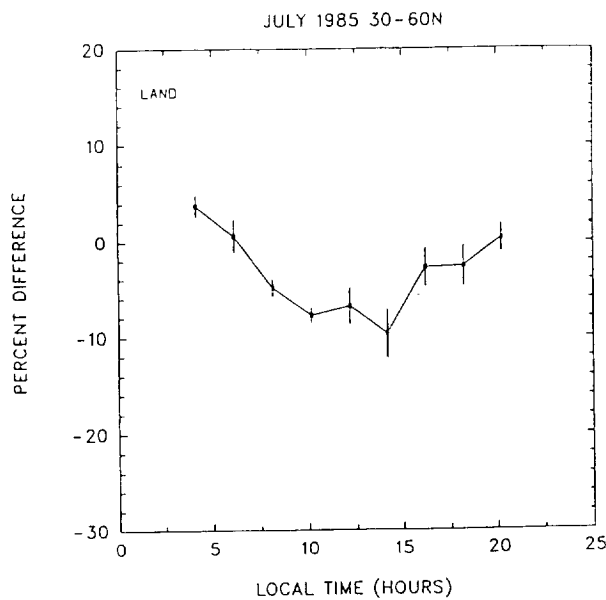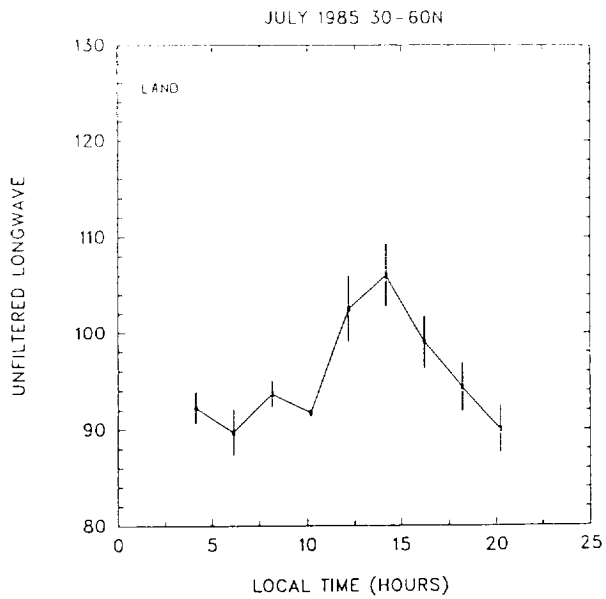
24

Figure 9. Unfiltered longwave radiances
observed by the ERBS scanner, a);
percent differences between observed
and calculated radiances, b) and surface
air temperatures from the NMC analyses,
c).

25

Table 2. Mean differences (computed – observed) and standard deviations in parentheses as a percent of the observed.

January 1986	Day		Night	
Surface Type	0Z	12Z	0Z	12Z
Land	-9.04 (4.92)	-10.73 (6.69)	-2.17 (3.95)	-4.03 (3.79)
Ocean	-2.95 (3.12)	-2.08 (2.35)	-4.39 (1.49)	-3.31 (1.69)
Desert	-4.37 (5.07)	-9.66 (7.08)	4.52 (5.11)	2.28 (6.40)

July 1985	Day		Night	
Surface Type	0Z	12Z	0Z	12Z
Land	-2.23 (3.84)	-5.56 (5.55)	-0.41 (2.87)	-2.48 (2.00)
Ocean	-2.77 (3.38)	-2.00 (2.29)	-2.62 (2.73)	-2.48 (1.79)
Desert	-3.18 (4.52)	-9.74 (5.72)	7.95 (4.76)	1.46 (2.62)

surface albedos, the anisotropy of the reflected radiation, subpixel scale variation in cloud liquid water concentrations and variations in droplet size all failed. Based on the work of Whitlock et al. (1988) and Staylor (1991) it was finally decided that the overriding cause of the discrepancy was the lack of calibration for the AVHRR. We attempted to calibrate the AVHRR 0.63-μm reflectivities through comparison of reflected radiances with those obtained simultaneously for collocated ERBE scanner fields of view.

The calibration of the AVHRR 0.63-μm reflectivities involves two parts. First, theoretical results were obtained for the slope and offset in the relationship

$$r_a = ar_e + b \qquad\qquad (4)$$

where r_a is the reflectivity measured by the AVHRR and r_e is the reflectivity, assuming isotropic reflection, obtained with the unfiltered ERBE scanner shortwave channel. Calculations of reflected unfiltered broadband reflectivities and the narrow 0.63 μm reflectivities associated with the AVHRR channel were performed with a radiative transfer model. The model was similar to the Lacis and Hansen (1974) parameterization. In the model, however, absorption by the Chappius band of ozone was explicitly allowed for using the absorption cross sections reported by Houghton (1979). Also, the nominal filter function for the AVHRR 0.63 μm channel was used (Kidwell, 1992).

Figure 11 shows least squares fits to (4). In the calculations, variations in the narrow and broadband reflectivities were created through variation in cloud optical depths. The optical depth of the cloud was varied from 0 to 64. The markers indicate reflectivities for the specific optical depths used in the calculations. The cloud-free background was assumed to be an ocean scene. The surface was assumed to be a diffuse reflector with an albedo of 0.06. In the calculations two column amounts of ozone were used. The upper curve is associated with a low column amount of ozone, 0.2 cm-STP, and the lower curve is associated with an upper column amount of ozone, 0.8 cm-STP. The lower column amount of ozone represents approximately half the climatological column amount found in the tropics and the upper column amount represents approximately twice the climatological value. So, the two curves represent upper and lower bounds to the relationship expected between AVHRR 0.63 μm and ERBE broadband reflectivities. Variation in water vapor had little effect on the values obtained for a and b in (4).
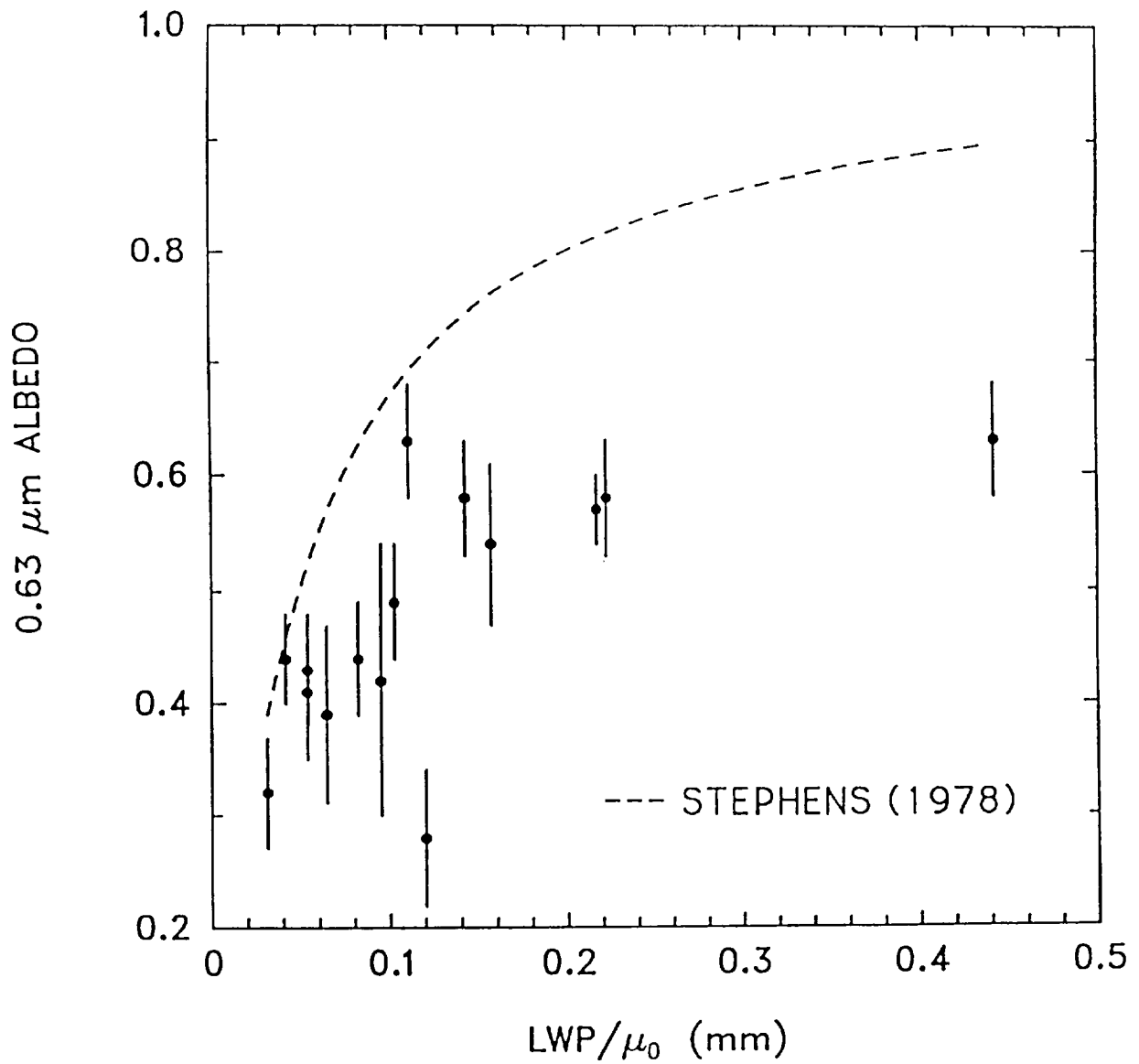
27

Figure 10. Observed and calculated 0.63-μm cloud albedos as a function of liquid water path for AVHRR and microwave radiometer observations taken during the 1987 FIRE Marine Stratocumulus Intensive Field Observations. The calculated albedos are based on the Stephens (1978) parameterization.

If the narrow to broadband conversion between the reflectivities were linear, there would be no offset, $b = 0$ in (4). Zero broadband reflectivity would accompany zero narrow band reflectivity. There is, however, a shift in the color of ocean scenes as the cloud optical depth varies from small values to large values. As a result the relationship is in fact slightly nonlinear. The offset is a ramification of the nonlinearity.

Allowing for the wide range of ozone column amounts the results of the calculations indicate that

$$r_a = (1.14 \pm 0.07)r_e - 2.0 \qquad (5)$$

where r_a and r_e are given in percent ($0 < r < 100$). The range in the column amount of ozone used in these calculations is unreasonably large. The likely range of the slope is probably closer to 5%. The actual value of the slope depends, of course, on the validity of the radiative transfer model which is unknown. Shine et al. (1984), however, obtained similar values.

The slope and offset also depend on solar zenith angle. The slope is large for overhead sun and small for the sun at low incident angles. The variation of the slope with solar zenith angle, however, falls within the variation given above for variation with ozone column amounts.

The theoretical slope and offset were compared with observed slopes and offsets. The observed slopes and offsets were obtained from the ERBE V5 Scene Identification Validation data. AVHRR radiances were collocated with ERBE scanner fields of view and allowance was made for the point spread function of the ERBE scanner. Radiances were collected from partially cloudy, mostly cloudy and overcast ocean scenes. AVHRR

reflectivities in the 0.63-μm channel were correlated with unfiltered shortwave reflectivities obtained with the ERBE scanner. The shortwave reflectivities were obtained assuming an isotropic reflecting surface. Figure 12 shows typical examples of these correlations for the NOAA-9 and NOAA-10 instruments.

Reasonably good correlations were obtained between the AVHRR 0.63-μm and ERBE unfiltered shortwave reflectivities. Figure 13 shows the slope for November 1985 obtained with the NOAA-9 satellite and for June 1988 for the NOAA-10 satellite. The values clustered when the correlation was high. Extraneous values of the slope occurred when the correlation was unusually low. The low values for the correlation coefficient occurred when either the ERBE scanner stuck or when the scene contained land which significantly altered the relative colors of the narrow and broadband observations. To avoid these problems, results were accumulated only in cases where the correlation coefficient exceeded 0.95. The results shown in Fig. 13 satisfied this condition.

Because the narrow and broadband observations were subject to differing degrees of absorption, we expected the relationship between the radiances to exhibit some bidirectional behavior. Figure 13 shows the slope as a function of satellite zenith angle. Values for the individual scene identification regions are indicated by different symbols. Clearly, any variation due to viewing geometry is masked by the natural variability which is due to shifts in ozone, water vapor and cloud properties. Consequently, we ignore any dependence on sun-satellite viewing geometry. Second, the results indicate that a single relationship holds for all regions. Again, natural variability within a single region is sufficient to mask any region to region variation. Consequently, a global relationship seems feasible.
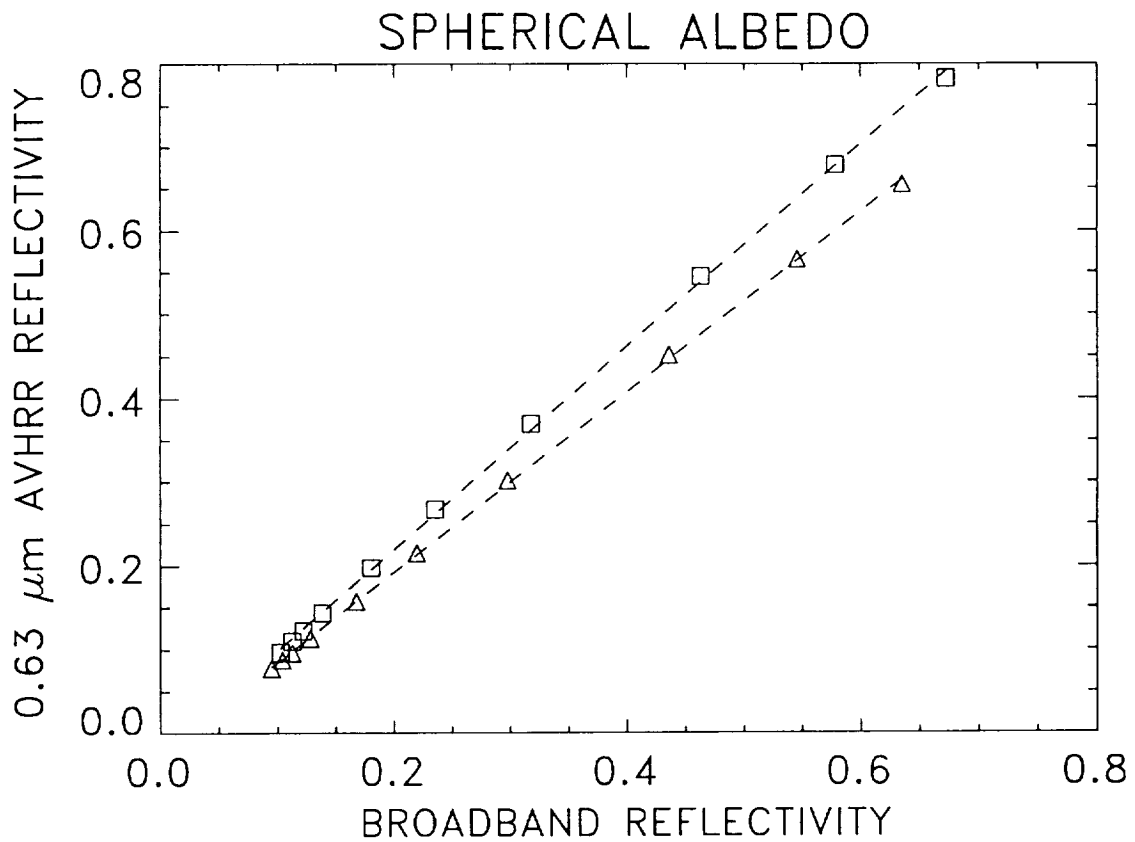
Figure 11. Narrow and broadband reflectivities calculated for clouds with visible optical depths ranging from 0 to 64, as indicated by the locations of the symbols. The upper curve (squares) is for an ozone column amount of 0.2 cm-STP and the lower curve (triangles) is for a column amount of 0.8 cm-STP. Midlatitude profiles for temperature andhumidity were used in the calculations.

Figure 14 gives the change in the slope with time for the NOAA-9 and NOAA-10 satellites for the months for which V-5 observations were available. The sensitivities of the AVHRR sensors for both satellites clearly degraded with time, although at different rates. Corrected calibration coefficients for the AVHRR were obtained using (4) and (5). Departures of the slopes and offsets from those obtained from theory were taken to indicate the required corrections.

The same procedures appear to be applicable to calibrating the 0.89-μm reflectivities obtained with the AVHRR. The near infrared reflectivities are used to obtain the normalized vegetation index (NDVI). This index is, of course, also subject to degradation of the sensor's sensitivity. Figure 15 shows correlations between 0.89-μm and broadband shortwave reflectivities like those shown in Fig. 12. The fits appear to be as good as those for the 0.63-μm and broadband reflectivities indicating that the same procedures can be used to obtain calibrated reflectivities at 0.89 μm. This work will be undertaken as part of an Interdisciplinary Science Team investigation supported by NASA's Earth Observing System program.

9.   Summary

New cloud algorithms have been developed using ERBE observations (Coakley and Bretherton, 1982; Coakley and Baldwin, 1984; Chang and Coakley, 1993; Lin and Coakley, 1993). Retrievals of cloud cover obtained with the spatial coherence method were used to assess the success of the ERBE MLE scene identification. While relatively large (> 15%) discrepancies in the reflected fluxes were found using the different scene identification methods for particular scene types, the net effect for regions in which all scene types were included was typically < 5% of the reflected flux estimated by the ERBE inversion scheme.

32
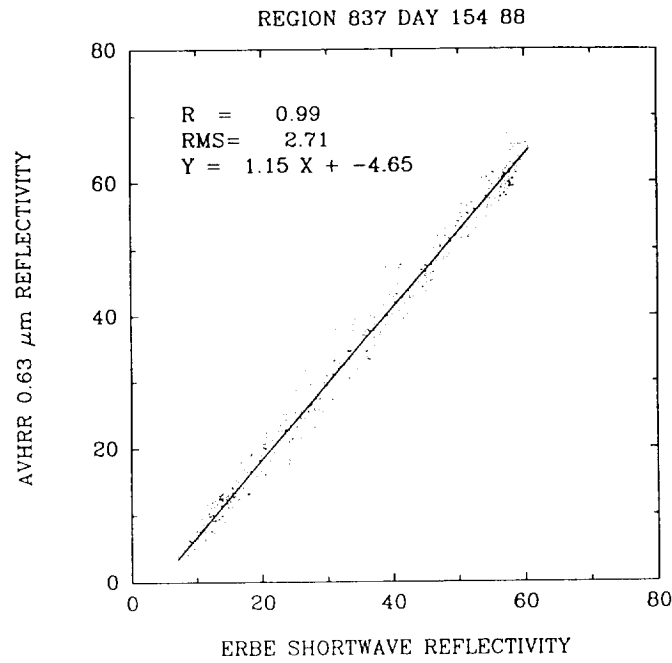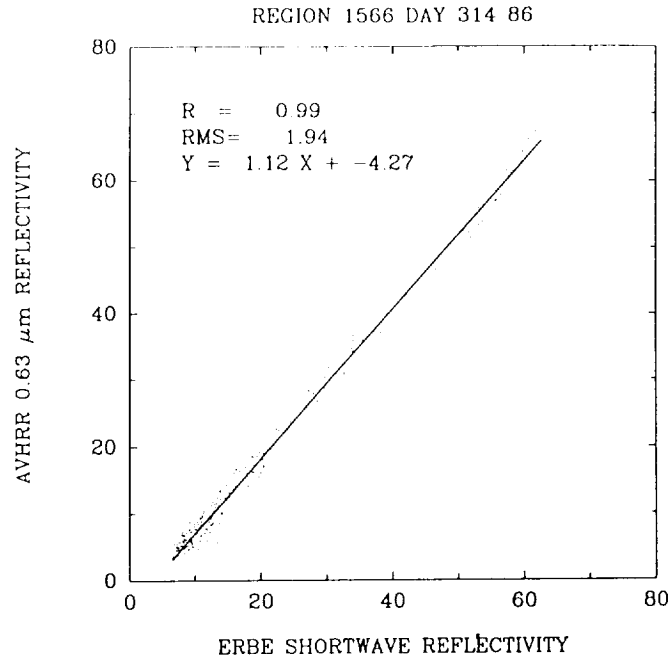
Figure 12. Shortwave and 0.63-μm reflectivities fit to (4) for NOAA-9 observations taken over ERBE V-5 region 1566 on 10 November 1986 and for NOAA-10 observations taken over V-5 region 837 on 2 June 1988.
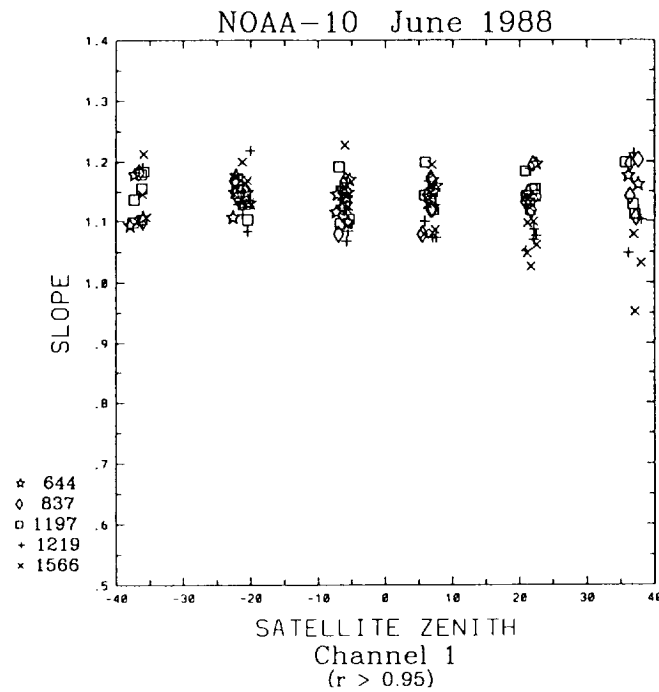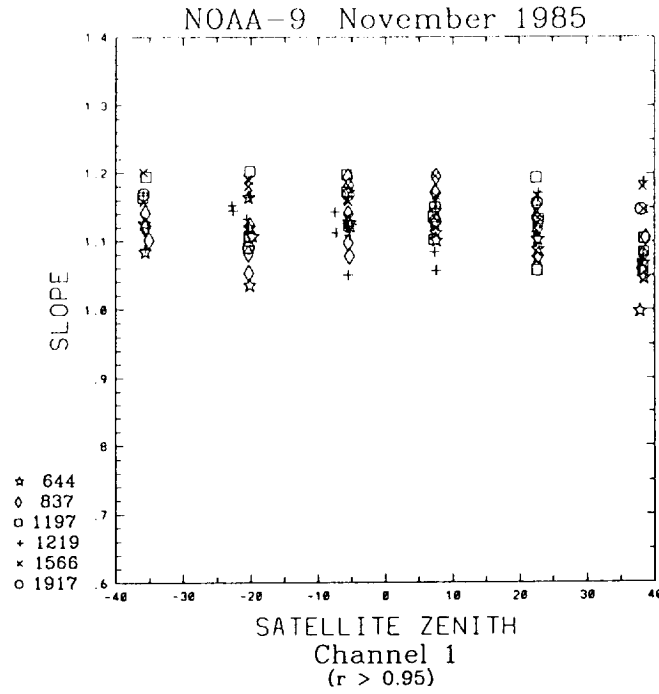
Figure 13. Slope in (4) obtained with the NOAA-9 instruments for November 1985 and with the NOAA-10 instruments for June 1988. The different symbols indicate the different ERBE V-5 regions. The slopes were derived from observations for partly cloudy and mostly cloudy ocean scenes and overcast scenes.

34
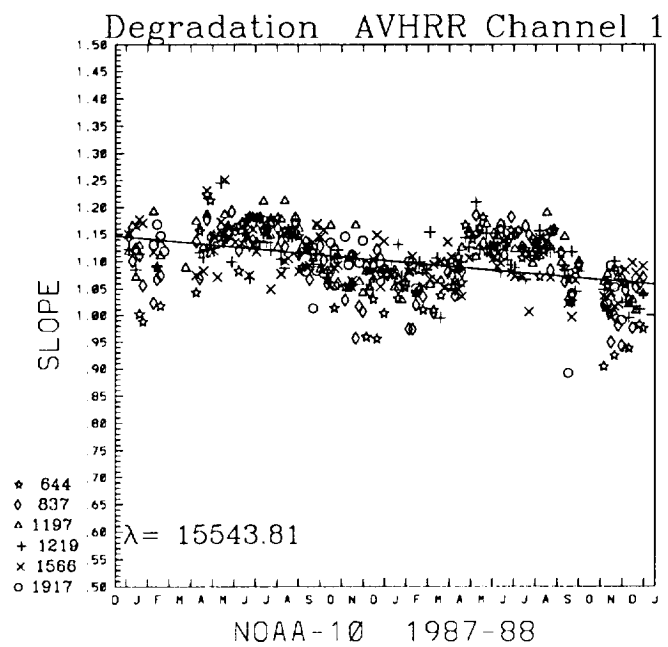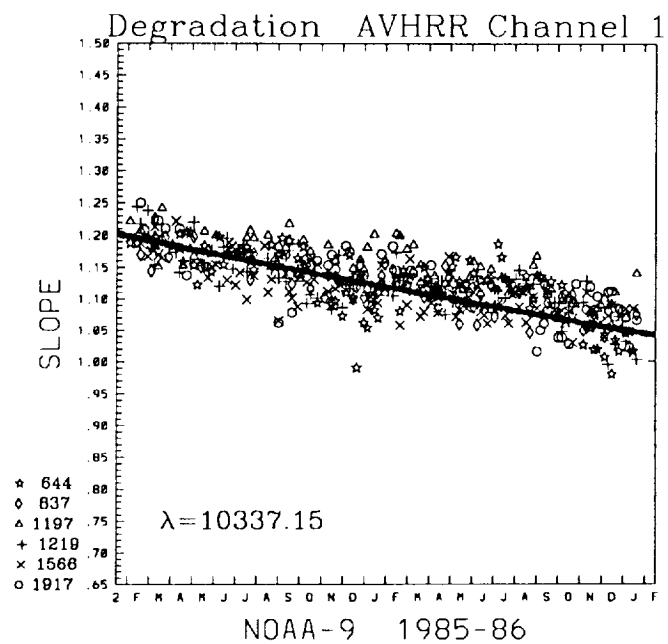
Figure 14. Slopes in (4) for NOAA-9 and NOAA-10.
λ is the exponential decay rate in days.

REGION 1566 DAY 314 86

R   =   0.99
RMS=   1.86
Y = 1.06 X + −4.91

REGION 837 DAY 154 88

R   =   0.99
RMS=   2.13
Y = 0.97 X + −4.46
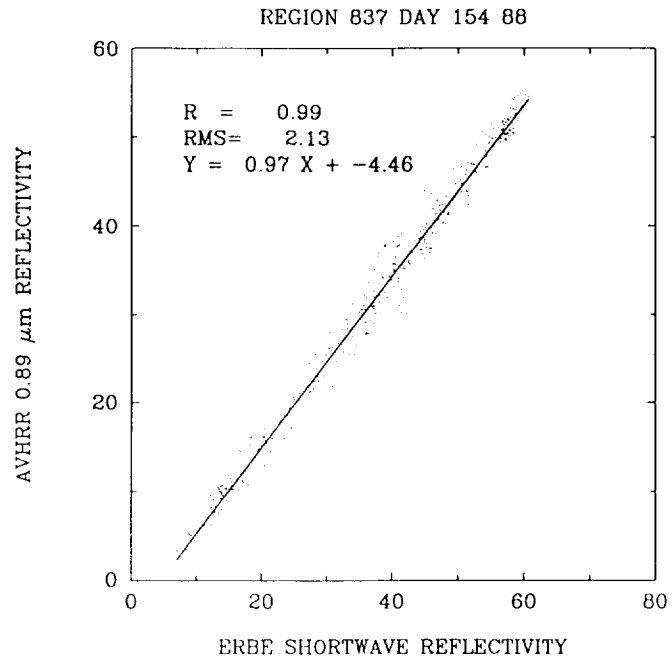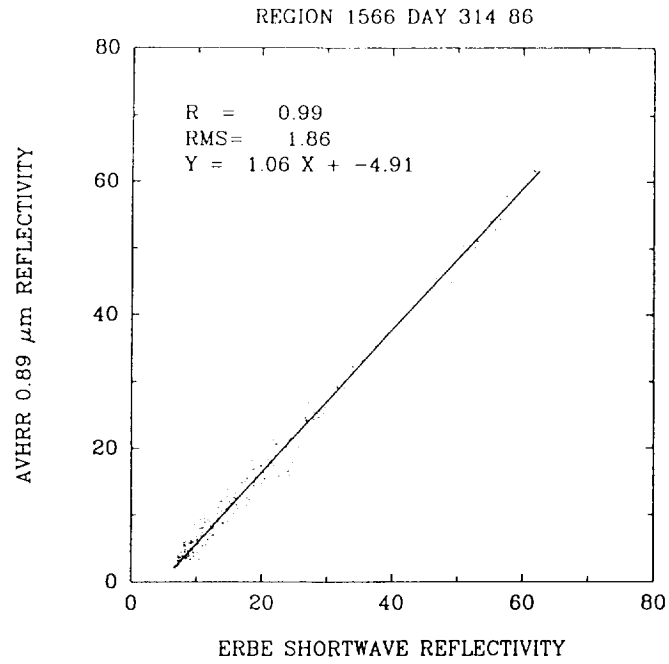
Figure 15. Same as Fig. 12 but for AVHRR reflectivities at 0.89 μm.

36

In addition to being used as a test bed for scene identification, the V-5 observations have been used to explore the properties of marine stratocumulus (Luo et al. 1994). Also, ongoing work involves the calibration of the AVHRR. 0.63 and 0.89-µm reflectivities which are used to form indices of surface vegetation.

Finally, longwave radiances were calculated using NMC analyzed temperature and humidity fields for regions that were collocated with ERBE scanner observations of clear regions. Calculations for ocean scenes were typically within 3% of the observed values. For land scenes the discrepancies were typically larger and exhibited a diurnal variation suggesting that the discrepancy was due to the surface skin temperature being significantly larger in the afternoon than the surface air temperature which is reported in the analyzed fields.

References

Baldwin, D.G. and J.A. Coakley, Jr., 1991: Consistency of Earth Radiation Budget Experiment bidirectional models and the observed anisotropy of reflected sunlight. *J. Geophys. Res.*, **96**, 5195-5207.

Chang, F-L., and J.A. Coakley, Jr., 1993: Estimating errors in fractional cloud cover obtained with infrared threshold methods. *J. Geophys. Res.*, **98**, 8825-8839.

Coakley, J.A., Jr., and F.P. Betherton, 1982: Cloud cover from high-resolution scanner data: Detecting and allowing for partially filled fields of view. *J. Geophys. Res.*, **87**, 4917-4932.

Coakley, J.A., Jr., and D.G. Baldwin, 1984: Towards the objective analysis of clouds from satellite imagery data, *J. Climate and Appl. Meteor.*, **23**, 1065-1099.

Coakley, J.A., Jr., 1990: Using spatial coherence to retrieve cloud properties: ERBE Experience and CERES Applications. *SPIE Proceedings, Long-Term Monitoring of the Earth's Radiation Budget*, B. Barkstrom, Ed., 119-127.

Coakley, J.A., Jr. and J.B. Snider, 1989: Observed reflectivities and liquid water content for marine stratocumulus. Preprints, AMS Symposium on the Role of Clouds in Atmospheric Chemistry and Global Climate, 175-177.

Harrison, E.F., P. Minnis, B.R. Barkstrom, V. Ramanathan, R.D. Cess and G.G. Gibson, 1990: Seasonal variation of cloud radiative forcing derived from the Earth Radiation Budget Experiment. *J. Geophys. Res.*, **95**, 18,687-18,704.

Houghton, J.T., 1977: *The Physics of Atmospheres.* Cambridge University Press.

Koffler, R.A., A.G. DeCotis and P.K. Rao, 1973: A procedure for estimating cloud amount and height from satellite infrared radiation data. *Mon. Wea. Rev.*, **101**, 240-243.

Lacis A.A., and J.E. Hansen, 1974: A parameterization for the absorption of solar radiation in the Earth's atmosphere. *J. Atmos. Sci.*, **31**, 118-133.

Lauritson, L., G.J. Nelson and F.W. Porto, 1979: Data extraction and calibration of TIROS-N/NOAA radiometers. *NOAA Technical Memorandum* NESS 107.

Lin, X. and J.A. Coakley, Jr., 1993: Retrieval of properties for semitransparent clouds from multispectral infrared imagery data. *J. Geophys. Res.*, **98**, 18,501-18,514.

Luo, G., X. Lin, and J.A. Coakley, Jr., 1994: 11-μm emissivities and droplet radii for marine stratocumulus, *J. Geophys. Res.*, **99**, 3685-3698.

Luther, F.M., R.G. Ellingson, Y. Fouquart, S. Fels, N.A. Scott and W.J. Wiscombe, 1988: Intercomparison of radiation codes in climate models (ICRCCM): Longwave clear-sky results--A workshop summary. *Bull. Amer. Meteor. Soc.*, **69**, 40-48.

Krueger, A.J. and R.A. Minzner, 1976: A mid-latitude ozone model for the 1976 U.S. Standard Atmosphere. *J. Geophys. Res.*, **81**, 4477-4481.

Reynolds, D.W. and T.H. Vonder Haar, 1977: A bi-spectral method for cloud parameter determination. *Mon. Wea. Rev.*, **105**, 446-457.

Rodgers C.D. and C.D. Walshaw, 1966: The computation of infrared cooling rate in planetary atmospheres. *Q. J. R. Meteor. Soc.*, **92**, 67-92.

Shenk, W.E. and V.V. Salomonson, 1972: A simulation study exploring the effects of sensor spatial resolution on estimates of cloud cover from satellites. *J. Appl. Meteor.*, **12**, 214-220.

Shine, K.P., A. Henderson-Sellers and A. Slingo, 1984: The influence of the spectral response of satellite sensors on estimates of broadband albedo. *Quart. J. R. Met. Soc.*, **110**, 1170-1179.

Staylor, W.P., 1990: Degradation rates of the AVHRR visible channel for the NOAA 6, 7 and 9 spacecraft. *J. Atmos. Ocean. Tech.*, **7**, 411-423.

Stephens, G.L., 1978: Radiation profiles in extended water clouds. II: Parameterization schemes. *J. Atmos. Sci.*, **35**, 2123-2132.

Stone, K.A., 1990: *Modeled and Observed Longwave Radiances at the Top of the Atmosphere*. M.S. Thesis. Department of Atmospheric Sciences, Oregon State University. 58 pp.

Stone K. and J.A. Coakley, Jr., 1990: Comparison of observed and modeled longwave radiances. Preprints, AMS Seventh Conference on Atmospheric Radiation, San Francisco. 134-136.

Suttles J.T., R.N. Green, P. Minnis, G.L. Smith, W.F. Staylor, B.A. Wielicki, I.J. Walker, D.F. Young, V.R. Taylor and L.L. Stowe, 1988: Angular radiation models for the earth-atmosphere system. Vol. I: Shortwave radiation. *NASA Ref. Publ. RP-1184*, 147 pp.

Suttles, J.T., B.A. Wielicki and S. Vemury, 1992: Top-of-atmosphere radiative fluxes: Validation of ERBE scanner inversion algorithm using Nimbus-7 ERB data. *J. Appl. Meteor.*, **31**, 784-796.

Taylor, V.R. and L.L. Stowe, 1984: Reflectance characteristics of uniform earth and cloud surfaces derived from Nimbus-7 ERB. *J. Geophys. Res.*, **89**, 4987-4996.

Wielicki B.A. and J.A. Coakley, Jr., 1981: Cloud retrieval using infrared sounder data: Error analysis. *J. Appl. Meteor.*, **20**, 157-169

Wielicki, B.A. and R.N. Green, 1989: Cloud identification for ERBE radiative flux retrieval. *J. Appl. Meteor.*, **28**, 1133-1146.

Wielicki, B.A., and L. Parker, 1992: On the determination of cloud cover from satellite sensors: The effect of sensor spatial resolution, *J. Geophys. Res.*, **97**, 12,799-12,823.

Whitlock, C.H., W.F. Staylor, G. Smith, R. Levin, R. Frouin, C. Gautier, P.M. Teillet, P.N. Slater, Y.J. Kaufman, B.N. Holben, S.R. Lecroy, 1988: AVHRR and VISSR satellite instrument calibration results for both cirrus and marine stratocumulus IFO periods. FIRE Science Results. NASA Conference Publication 3083, pp. 141-146.

Ye, Q., 1993: *The Spatial-Scale Dependence of the Observed Anisotropy of Reflected and Emitted Radiation.* PhD Thesis. College of Oceanic and Atmospheric Sciences. Oregon State University. 159 pp.

REPORT DOCUMENTATION PAGE

1. AGENCY USE ONLY *(Leave blank)*	2. REPORT DATE 7 March 1994	3. REPORT TYPE AND DATES COVERED Contractor Report

4. TITLE AND SUBTITLE Science Support for the Earth Radiation Budget Experiment	5. FUNDING NUMBERS C NAS1-18992 WU 665-45-20-01

6. AUTHOR(S) James A. Coakley, Jr.	

7. PERFORMING ORGANIZATION NAME(S) AND ADDRESS(ES) Oregon State University College of Oceanic and Atmospheric Sciences Corvallis, OR 97331	8. PERFORMING ORGANIZATION REPORT NUMBER

9. SPONSORING/MONITORING AGENCY NAME(S) AND ADDRESS(ES) National Aeronautics and Space Administration Langley Research Center Hampton, VA 23681-0001	10. SPONSORING/MONITORING AGENCY REPORT NUMBER NASA CR-191600

11. SUPPLEMENTARY NOTES
Langley Technical Monitor: Robert J. Keynton
Final Report

12a. DISTRIBUTION/AVAILABILITY STATEMENT Unclassified-Unlimited Subject Category 47	12b. DISTRIBUTION CODE

13. ABSTRACT *(Maximum 200 words)*

The work undertaken as part of the Earth Radiation Budget Experiment (ERBE) included the following major components: 1) The development and application of a new cloud retrieval scheme to assess errors in the radiative fluxes arising from errors in the ERBE identification of cloud conditions. 2) The comparison of the anisotropy of reflected sunlight and emitted thermal radiation with the anisotropy predicted by the Angular Dependence Models (ADMs) used in to obtain the radiative fluxes. Additional studies included the comparison of calculated longwave cloud-free radiances with those observed by the ERBE scanner and the use of ERBE scanner data to track the calibration of the shortwave channels of the Advanced Very High Resolution Radiometer (AVHRR). Major findings included: 1) The misidentification of cloud conditions by the ERBE scene identification algorithm could cause 15% errors in the shortwave flux reflected by certain scene types. For regions containing mixtures of scene types, the errors were typically less than 5%. 2) The anisotropies of the shortwave and longwave radiances exhibited a spatial scale dependence which, because of the growth of the scanner field of view from nadir to limb, gave rise to a view zenith angle dependent bias in the radiative fluxes.

| 14. SUBJECT TERMS
Retrieval of cloud properties; Scene identification; Anisotropy of reflected and emitted radiances; Calibration of AVHRR shortwave channels | 15. NUMBER OF PAGES
44 |
	16. PRICE CODE

17. SECURITY CLASSIFICATION OF REPORT Unclassified	18. SECURITY CLASSIFICATION OF THIS PAGE Unclassified	19. SECURITY CLASSIFICATION OF ABSTRACT	20. LIMITATION OF ABSTRACT